Flow Turbulence Combust (2016) 97:1071–1093
DOI 10.1007/s10494-016-9759-9

Transport Mechanism of Interface Turbulence over Porous and Rough Walls

Yusuke Kuwata[1,2] · **Kazuhiko Suga**[1]

Received: 23 December 2015 / Accepted: 5 August 2016 / Published online: 18 August 2016

Abstract To understand turbulent transport mechanisms of interface turbulence over porous and rough walls, statistical analyses using direct numerical simulation (DNS) data are carried out at a bulk Reynolds number of 3000. The presently considered porous wall, whose porosity is 0.71, consists of interconnected staggered cube arrays and the rough wall has the same surface structure. Through quadrant and budget term analyses, the transport mechanisms of the plane averaged Reynolds stress are investigated and mutual dependency between turbulence and dispersion is elucidated. Moreover, the influence of the Kelvin-Helmholtz instability on turbulent transport is clarified.

Keywords Direct numerical simulation · Lattice Boltzmann method · Turbulent channel flow · Porous media · Double averaged second moments · Budget terms

List of Symbols

C_f	bottom-wall friction factor
C_f^t	top-wall friction factor
d	zero-plane displacement
D	cube size
D^*	$D^* = L/2$
h	porous or rough wall thickness
h_r	roughness height
H	channel height
k	plane averaged turbulent kinetic energy : $k = R_{kk}/2$

✉ Kazuhiko Suga
suga@me.osakafu-u.ac.jp

[1] Department of Mechanical Engineering, Osaka Prefecture University, Sakai, Osaka 599-8531, Japan

[2] Present address: Department of Mechanical Engineering, Tokyo University of Science, 2641 Yamazaki, Noda-shi, Chiba 278-8510, Japan

K	permeability
$\mathcal{K}$	plane-dispersion energy : $\mathcal{K} = \mathcal{T}_{kk}/2$
L	cube-row pitch
p	pressure
R_{ij}	plane averaged Reynolds stress: $\overline{\left[u_i' u_j'\right]^f}$
R_{e_b}	bulk Reynolds number: $R_{e_b} = U_b H/\nu$
R_{e_τ}	bottom-wall friction Reynolds number: $R_{e_\tau} = u_\tau \delta/\nu$
$R_{e_\tau^t}$	top-wall friction Reynolds number: $R_{e_\tau^t} = u_\tau^t \delta^t/\nu$
t	time
$\mathcal{T}_{ij}$	plane-dispersive covariance : $\left[\tilde{\overline{u_i}}\,\tilde{\overline{u_j}}\right]^f$
u_i	velocity
u_τ	bottom-wall friction velocity
u_τ^t	top-wall friction velocity
U_b	bulk mean velocity
x	streamwise coordinate
y	wall-normal coordinate
z	spanwise coordinate
δ	bottom-wall boundary layer thickness
δ^t	top-wall boundary layer thickness
Δ^c	coarser grid spacing
Δ^f	finer grid spacing
κ	Kármán constant
ν	kinematic viscosity
ρ	fluid density
φ	porosity
ϕ	variable
$\overline{\phi}$	Reynolds averaged value of ϕ
ϕ'	fluctuation of ϕ : $\phi - \overline{\phi}$
$[\phi]^f$	plane averaged value of ϕ
$\tilde{\phi}$	dispersion of ϕ : $\phi - [\phi]^f$
ψ	surface porosity
$(\,)^+$	normalized value by u_τ
$(\,)^{t+}$	normalized value by u_τ^t

1 Introduction

Nuclear reactor cores, catalytic converters, metal foam heat exchangers, vegetation and urban canopies can be considered to be porous media. Since interface turbulence over the porous medium plays an important role for heat and mass transfer of the system, understanding the turbulent transport mechanisms helps us to control its performance. Accordingly, many studies on the turbulent transport processes inside the interface regions of porous media have been performed.

For flows over vegetation canopies, some experimental studies paid attention to production, diffusion and dissipation processes of the turbulent kinetic energy. By sonic anemometry measurements, Meyers and Baldocchi [19] carried out a budget term analysis for the turbulent kinetic energy equation. They concluded that the mean shear production

was dominant near the canopy interface whilst the 'wake production' (mean dispersive-shear production) exceeded the mean shear production inside the canopy. Katul [10] performed triaxial sonic anemometer measurements to investigate behaviours of triple velocity correlations and reported that the triple moment related to the vertical turbulent diffusion process of the Reynolds shear stress became significant just above the interface. By acoustic and laser Doppler velocimetries, Nepf [20] measured the drag force, turbulent and 'mechanical diffusion' (transport by dispersion) terms of the scaler transport within a vegetation canopy. The experiments showed that the turbulence intensity was mainly dependent on the drag. It was found that as the vegetation density increased (or the porosity decreased), the turbulent diffusion was reduced due to the reduction of an eddy scale whilst the mechanical diffusion, which arose from the velocity dispersion, became significant. Nezu and Sanjou [21] measured aquatic vegetation canopy flows by laser Doppler and particle image velocimetries. Their budget term analysis for the turbulent kinetic energy equation revealed that the turbulent diffusion played an essential role in the mixing layer. For flows over permeable beds, Pokrajac and Manes [23] and Manes et al. [18] measured turbulent open channel flows over a porous bed composed of glass spheres by particle image velocimetry and an ultrasonic velocity profiler. They concluded that turbulent kinetic energy was transported toward the lower bed mainly by pressure fluctuations whereas the transport by turbulent velocity fluctuations was limited to a thinner layer in the upper part of the bed.

From those experimental studies, it was found that, in the interface regions of porous media, the mean shear production was the major process and the turbulent diffusion transported the energy downward to the porous layer whilst the dispersion production became dominant inside the layer. However, accuracy and reliability of the measured data were sometimes limited to the clear flow regions because of the difficulty of measurements inside porous media. Consequently, behaviours of higher order turbulent correlations such as the budget terms of the Reynolds stress equations were not fully investigated and the detailed turbulent transport mechanism in the porous and fluid interface region was not realized very well.

Accordingly, several large eddy simulation (LES) and direct numerical simulation (DNS) studies have been attempted. Since enormous computational costs are required to resolve the complex porous structures, the volume averaged Navier-Stokes (VANS) equations of Whitaker [29, 30] were sometimes applied to the porous regions. Dwyer et al. [6] conducted LES for flows over a modelled forest and investigated the turbulent kinetic energy budgets. As the forest permeability increased, turbulence was more enhanced due to the increased mean shear production. Their results showed that the turbulent diffusion worked near the interface whereas the pressure diffusion transported the energy deeply inside the forest. For porous-walled channels, Breugem et al. [2] performed a DNS study. They also applied the VANS equations to model the porous wall region and concluded that the wall-normal and spanwise Reynolds stresses were substantially enhanced near a highly permeable wall because of the significant redistribution from the streamwise component. Due to the weakened wall-blocking effect near the interface, the viscous diffusion became less important whereas the turbulent diffusion transported the wall-normal Reynolds stress inside the porous media. However, since their VANS equations included a model for the drag force term and neglected the effect of the dispersion, it may be considered that the turbulence transport mechanisms around and inside the porous layer were not precisely reproduced. They also performed another DNS study resolving each porous element [1]. Although root mean square values of turbulence fluctuations were reported, information of the budget terms of turbulent transport equations in the resolved porous layer was not provided. Recently, Chandesris et al. [3] also performed a full DNS study for low Prandtl number

(Pr= 0.1) heat transfer fields with the same flow conditions as those of Breugem et al. [2] resolving the model porous structure. Since their focus was on heat transfer, they did not provide any further information on turbulent flow physics than that in Ref. [2].

As described above, although several important pieces of information of the interface turbulence transport have been delivered, it can be said that many other aspects are still unrevealed. Hence, to reveal more the flow physics of interface turbulence over a porous wall and to clarify the effect of the wall permeability on turbulence, the present authors carried out a full DNS study of turbulent porous- and rough-walled channel flows (Kuwata and Suga [15]). The porous wall consisted of staggered cube arrays in which solid cubes were interconnected and the same solid structure was considered for the rough wall. To directly treat the porous structure, the D3Q27 multiple relaxation time (MRT) lattice Boltzmann method (LBM) [26] with the imbalance-correction local grid-refinement method [14] was employed for the turbulent flow simulation. The study focused on the presence and the characteristics of pressure perturbations induced by the Kelvin-Helmholtz (K-H) instability over the porous layer. Due to the pressure perturbations, it was confirmed that the turbulent coherent structure was shredded over the porous layer and large scale intermittent fluctuations were induced inside the porous layer. It was also confirmed that the intensified wall-normal and spanwise velocity fluctuations over the porous layer were due to the K-H instability and the most energy containing perturbations were of the wavelength of 550 wall units. In the present study, to discuss further the detailed transport mechanism of interface turbulence statistically, quadrant and budget term analyses of the second moments are carried out.

2 DNS by the D3Q27 MRT LBM

In our previous report [15], the time-dependent flow fields were simulated by the LBM since it has many distinctive computational features such as easiness for parallelization and applicability to complex geometries. The lattice Boltzmann equation can be obtained by discretizing the velocity space of the Boltzmann equation into a finite number of discrete velocities $\boldsymbol{\xi}_\alpha\{\alpha = 0, \cdots, Q-1\}$. There are several discrete velocity models for three-dimensional flows such as the D3Q15, D3Q19 and D3Q27 models. It was reported that although unphysical spurious currents were sometimes visible by the D3Q15 and D3Q19 models in axisymmetric flows, they were effectively suppressed by the D3Q27 model [9, 13, 31]. Also, to ensure the numerical stability for high Reynolds number flows, it is effective to apply the MRT scheme [5]. Accordingly, our study employed the D3Q27 MRT-LBM [26]. The time evolution of the distribution function of the MRT-LBM can be written as

$$|\, \boldsymbol{f}(\boldsymbol{x}+\boldsymbol{\xi}_\alpha \delta t, t+\delta t)\rangle - |\, \boldsymbol{f}(\boldsymbol{x},t)\rangle = -\boldsymbol{M}^{-1}\hat{\boldsymbol{S}}\left[|\, \boldsymbol{m}(\boldsymbol{x},t)\rangle - |\, \boldsymbol{m}^{\boldsymbol{eq}}(\boldsymbol{x},t)\rangle\right], \tag{1}$$

where the notation such as $|\boldsymbol{f}\rangle$ is $|\boldsymbol{f}\rangle = (f_0, f_1, \cdots, f_{Q-1})^T$ and δt is the time step. Note that for the D3Q27 model, $Q = 27$. The discrete velocity components $\boldsymbol{\xi}_\alpha$ for the D3Q27 model are listed in Table 1. The matrix $\boldsymbol{M}$ is a $Q \times Q$ matrix which linearly transforms the distribution functions to the moments as $|\boldsymbol{m}\rangle = \boldsymbol{M}|\boldsymbol{f}\rangle$. The equilibrium moment $\boldsymbol{m}^{\boldsymbol{eq}}$ is obtained as $\left|\boldsymbol{m}^{\boldsymbol{eq}}\right\rangle = \boldsymbol{M}\left|\boldsymbol{f}^{\boldsymbol{eq}}\right\rangle$ with

$$f_\alpha^{eq} = w_\alpha\left(\rho + \rho_0\left[\frac{\boldsymbol{\xi}_\alpha\cdot\boldsymbol{u}}{c_s^2} + \frac{(\boldsymbol{\xi}_\alpha\cdot\boldsymbol{u})^2 - c_s^2|\boldsymbol{u}|^2}{2c_s^4}\right]\right), \tag{2}$$

Table 1 Parameters of the D3Q27 discrete velocity model

Model	c_s/c	$\boldsymbol{\xi}_\alpha/c$	w_α
D3Q27	$1/\sqrt{3}$	$(0,0,0)$	$8/27(\alpha=0)$
		$(\pm1,0,0),(0,\pm1,0),(0,0,\pm1)$	$2/27(\alpha=1,\cdots,6)$
		$(\pm1,\pm1,0),(\pm1,0,\pm1),(0,\pm1,\pm1)$	$1/54(\alpha=7,\cdots,18)$
		$(\pm1,\pm1,\pm1)$	$1/216(\alpha=19,\cdots,26)$

where $\boldsymbol{u}$ is the fluid velocity and ρ is expressed as the sum of constant and fluctuation values: $\rho = \rho_0 + \delta\rho$ [8]. The sound speed is $c_s/c = 1/\sqrt{3}$ with $c = \Delta/\delta t$ where Δ is the lattice spacing and the values of w_α are listed in Table 1. The equilibrium moments

Table 2 Equilibrium moments

$$
\begin{aligned}
m_0^{eq} &= \rho \equiv \textstyle\sum_{\alpha=0}^{26} f_\alpha^{eq}\\
m_1^{eq} &= j_x \equiv \textstyle\sum_{\alpha=0}^{26} f_\alpha^{eq}\xi_{\alpha x}\\
m_2^{eq} &= j_y \equiv \textstyle\sum_{\alpha=0}^{26} f_\alpha^{eq}\xi_{\alpha y}\\
m_3^{eq} &= j_z \equiv \textstyle\sum_{\alpha=0}^{26} f_\alpha^{eq}\xi_{\alpha z}\\
m_4^{eq} &= e \equiv \textstyle\sum_{\alpha=0}^{26}\left(\xi_{\alpha x}^2+\xi_{\alpha y}^2+\xi_{\alpha z}^2\right) f_\alpha^{eq}\\
m_5^{eq} &= XX \equiv \textstyle\sum_{\alpha=0}^{26}\left(2\xi_{\alpha x}^2-\xi_{\alpha y}^2-\xi_{\alpha z}^2\right) f_\alpha^{eq}\\
m_6^{eq} &= WW \equiv \textstyle\sum_{\alpha=0}^{26}\left(\xi_{\alpha y}^2-\xi_{\alpha z}^2\right) f_\alpha^{eq}\\
m_7^{eq} &= XY \equiv \textstyle\sum_{\alpha=0}^{26}\left(\xi_{\alpha x}\xi_{\alpha y}\right) f_\alpha^{eq}\\
m_8^{eq} &= YZ \equiv \textstyle\sum_{\alpha=0}^{26}\left(\xi_{\alpha y}\xi_{\alpha z}\right) f_\alpha^{eq}\\
m_9^{eq} &= ZX \equiv \textstyle\sum_{\alpha=0}^{26}\left(\xi_{\alpha z}\xi_{\alpha x}\right) f_\alpha^{eq}\\
m_{10}^{eq} &= \varphi_x \equiv 3\textstyle\sum_{\alpha=0}^{26}\left(\xi_{\alpha x}^2+\xi_{\alpha y}^2+\xi_{\alpha z}^2\right)\xi_{\alpha x} f_\alpha^{eq}\\
m_{11}^{eq} &= \varphi_y \equiv 3\textstyle\sum_{\alpha=0}^{26}\left(\xi_{\alpha x}^2+\xi_{\alpha y}^2+\xi_{\alpha z}^2\right)\xi_{\alpha y} f_\alpha^{eq}\\
m_{12}^{eq} &= \varphi_z \equiv 3\textstyle\sum_{\alpha=0}^{26}\left(\xi_{\alpha x}^2+\xi_{\alpha y}^2+\xi_{\alpha z}^2\right)\xi_{\alpha z} f_\alpha^{eq}\\
m_{13}^{eq} &= \psi_x \equiv \tfrac{9}{2}\textstyle\sum_{\alpha=0}^{26}\left(\xi_{\alpha x}^2+\xi_{\alpha y}^2+\xi_{\alpha z}^2\right)^2\xi_{\alpha x} f_\alpha^{eq}\\
m_{14}^{eq} &= \psi_y \equiv \tfrac{9}{2}\textstyle\sum_{\alpha=0}^{26}\left(\xi_{\alpha x}^2+\xi_{\alpha y}^2+\xi_{\alpha z}^2\right)^2\xi_{\alpha y} f_\alpha^{eq}\\
m_{15}^{eq} &= \psi_z \equiv \tfrac{9}{2}\textstyle\sum_{\alpha=0}^{26}\left(\xi_{\alpha x}^2+\xi_{\alpha y}^2+\xi_{\alpha z}^2\right)^2\xi_{\alpha z} f_\alpha^{eq}\\
m_{16}^{eq} &= \varepsilon \equiv \tfrac{3}{2}\textstyle\sum_{\alpha=0}^{26}\left(\xi_{\alpha x}^2+\xi_{\alpha y}^2+\xi_{\alpha z}^2\right)^2 f_\alpha^{eq}\\
m_{17}^{eq} &= e_3 \equiv \tfrac{9}{2}\textstyle\sum_{\alpha=0}^{26}\left(\xi_{\alpha x}^2+\xi_{\alpha y}^2+\xi_{\alpha z}^2\right)^3 f_\alpha^{eq}\\
m_{18}^{eq} &= XX_e \equiv \textstyle\sum_{\alpha=0}^{26}\left(2\xi_{\alpha x}^2-\xi_{\alpha y}^2-\xi_{\alpha z}^2\right)\left(\xi_{\alpha x}^2+\xi_{\alpha y}^2+\xi_{\alpha z}^2\right) f_\alpha^{eq}\\
m_{19}^{eq} &= WW_e \equiv \textstyle\sum_{\alpha=0}^{26}\left(\xi_{\alpha y}^2-\xi_{\alpha z}^2\right)\left(\xi_{\alpha x}^2+\xi_{\alpha y}^2+\xi_{\alpha z}^2\right) f_\alpha^{eq}\\
m_{20}^{eq} &= XY_e \equiv \textstyle\sum_{\alpha=0}^{26}\left(\xi_{\alpha x}\xi_{\alpha y}\right)\left(\xi_{\alpha x}^2+\xi_{\alpha y}^2+\xi_{\alpha z}^2\right) f_\alpha^{eq}\\
m_{21}^{eq} &= YZ_e \equiv \textstyle\sum_{\alpha=0}^{26}\left(\xi_{\alpha y}\xi_{\alpha z}\right)\left(\xi_{\alpha x}^2+\xi_{\alpha y}^2+\xi_{\alpha z}^2\right) f_\alpha^{eq}\\
m_{22}^{eq} &= ZX_e \equiv \textstyle\sum_{\alpha=0}^{26}\left(\xi_{\alpha z}\xi_{\alpha x}\right)\left(\xi_{\alpha x}^2+\xi_{\alpha y}^2+\xi_{\alpha z}^2\right) f_\alpha^{eq}\\
m_{23}^{eq} &= \tau_x \equiv \textstyle\sum_{\alpha=0}^{26}\xi_{\alpha x}\left(\xi_{\alpha y}^2-\xi_{\alpha z}^2\right) f_\alpha^{eq}\\
m_{24}^{eq} &= \tau_y \equiv \textstyle\sum_{\alpha=0}^{26}\xi_{\alpha y}\left(\xi_{\alpha z}^2-\xi_{\alpha x}^2\right) f_\alpha^{eq}\\
m_{25}^{eq} &= \tau_z \equiv \textstyle\sum_{\alpha=0}^{26}\xi_{\alpha z}\left(\xi_{\alpha x}^2-\xi_{\alpha y}^2\right) f_\alpha^{eq}\\
m_{26}^{eq} &= XYZ \equiv \textstyle\sum_{\alpha=0}^{26}\left(\xi_{\alpha x}\xi_{\alpha y}\xi_{\alpha z}\right) f_\alpha^{eq}
\end{aligned}
$$

ρ: density, j_x, j_y, j_z : momentum, e : kinetic energy, XX, WW, XY, YZ, ZX : second-order tensors, $\varphi_x, \varphi_y, \varphi_z$: flux of the energy, ψ_x, ψ_y, ψ_z : flux of the square of the energy, ε : square of the energy, e_3 : cube of the energy, XX_e, WW_e : product of XX and WW by the energy, XY_e, YZ_e, ZX_e : extra-diagonal second-order moments of the energy, τ_x, τ_y, τ_z : third-order pseudo vector, XYZ : third-order totally antisymmetric tensor.

and the transformation matrix are shown in Tables 2 and 3. The collision matrix $\hat{\boldsymbol{S}}$ is diagonal:

$$\hat{\boldsymbol{S}} \equiv diag(0, 0, 0, 0, s_4, s_5, s_5, s_7, s_7, s_7, s_{10}, s_{10}, s_{10}, s_{13}, s_{13}, s_{13}, s_{16}, s_{17}, s_{18}, s_{18}, s_{20}, s_{20}, s_{20}, s_{23}, s_{23}, s_{23}, s_{26}). \tag{3}$$

The relaxation parameters optimized in Ref.[26] are

$$s_4 = 1.54, \quad s_5 = s_7, \quad s_{10} = 1.5, \quad s_{13} = 1.83, \quad s_{16} = 1.4, \quad s_{17} = 1.61, \quad s_{18} = s_{20} = 1.98, \quad s_{23} = s_{26} = 1.74. \tag{4}$$

The relaxation parameters s_5 and s_7 are related to the kinematic viscosity ν,

$$\nu = c_s^2 \left(\frac{1}{s_5} - \frac{1}{2} \right) \delta t = c_s^2 \left(\frac{1}{s_7} - \frac{1}{2} \right) \delta t. \tag{5}$$

The accuracy of this D3Q27 MRT-LBM for the turbulent channel flow of Kim et al. [11] was confirmed to be equivalent to that of the spectral method. See Suga et al. [26] for the details.

3 Flow Geometry and Computational Conditions

Figure 1a illustrates the geometry of the porous-walled channel. The channel bottom wall was made of a porous medium whilst a smooth surface was considered for the top wall. The

Table 3 27×27 transformation matrix

$\mathbf{M} =$

1	1	1	1	1	1	1	1	1	1	1	1	1	1	1	1	1	1	1	1	1	1	1	1	1	1	1	1
1	0	−1	0	0	0	1	−1	−1	1	1	0	−1	0	1	0	−1	0	1	−1	−1	1	1	−1	−1	1	0	
0	1	0	−1	0	0	1	1	−1	−1	0	1	0	−1	0	1	0	−1	1	1	−1	−1	1	1	−1	−1	0	
0	0	0	0	1	−1	0	0	0	0	1	1	1	1	−1	−1	−1	−1	1	1	1	1	−1	−1	−1	−1	0	
−1	−1	−1	−1	−1	−1	0	0	0	0	0	0	0	0	0	0	0	0	1	1	1	1	1	1	1	1	−2	
2	−1	2	−1	−1	−1	1	1	1	1	1	−2	1	−2	1	−2	1	−2	0	0	0	0	0	0	0	0	0	
0	1	0	1	−1	−1	1	1	1	1	−1	0	−1	0	−1	0	−1	0	0	0	0	0	0	0	0	0	0	
0	0	0	0	0	0	1	−1	1	−1	0	0	0	0	0	0	0	0	1	−1	1	−1	1	−1	1	−1	0	
0	0	0	0	0	0	0	0	0	0	0	1	0	−1	0	−1	0	1	1	1	−1	−1	−1	−1	1	1	0	
0	0	0	0	0	0	0	0	0	0	1	0	−1	0	−1	0	1	0	1	−1	−1	1	−1	1	1	−1	0	
−4	0	4	0	0	0	−1	1	1	−1	−1	0	1	0	−1	0	1	0	2	−2	−2	2	2	−2	−2	2	0	
0	−4	0	4	0	0	−1	−1	1	1	0	−1	0	1	0	−1	0	1	2	2	−2	−2	2	2	−2	−2	0	
0	0	0	0	−4	4	0	0	0	0	−1	−1	−1	−1	1	1	1	1	2	2	2	2	−2	−2	−2	−2	0	
4	0	−4	0	0	0	−2	2	2	−2	−2	0	2	0	−2	0	2	0	1	−1	−1	1	1	−1	−1	1	0	
0	4	0	−4	0	0	−2	−2	2	2	0	−2	0	2	0	−2	0	2	1	1	−1	−1	1	1	−1	−1	0	
0	0	0	0	4	−4	0	0	0	0	−2	−2	−2	−2	2	2	2	2	1	1	1	1	−1	−1	−1	−1	0	
0	0	0	0	0	0	−1	−1	−1	−1	−1	−1	−1	−1	−1	−1	−1	−1	1	1	1	1	1	1	1	1	4	
4	4	4	4	4	4	−2	−2	−2	−2	−2	−2	−2	−2	−2	−2	−2	−2	1	1	1	1	1	1	1	1	−8	
−4	2	−4	2	2	2	1	1	1	1	1	−2	1	−2	1	−2	1	−2	0	0	0	0	0	0	0	0	0	
0	−2	0	−2	2	2	1	1	1	1	−1	0	−1	0	−1	0	−1	0	0	0	0	0	0	0	0	0	0	
0	0	0	0	0	0	−2	2	−2	2	0	0	0	0	0	0	0	0	1	−1	1	−1	1	−1	1	−1	0	
0	0	0	0	0	0	0	0	0	0	0	−2	0	2	0	2	0	−2	1	1	−1	−1	−1	−1	1	1	0	
0	0	0	0	0	0	0	0	0	0	−2	0	2	0	2	0	−2	0	1	−1	−1	1	−1	1	1	−1	0	
0	0	0	0	0	0	1	−1	−1	1	−1	0	1	0	−1	0	1	0	0	0	0	0	0	0	0	0	0	
0	0	0	0	0	0	−1	−1	1	1	0	1	0	−1	0	1	0	−1	0	0	0	0	0	0	0	0	0	
0	0	0	0	0	0	0	0	0	0	1	−1	1	−1	−1	1	−1	1	0	0	0	0	0	0	0	0	0	
0	0	0	0	0	0	0	0	0	0	0	0	0	0	0	0	0	0	1	−1	1	−1	−1	1	−1	1	0	

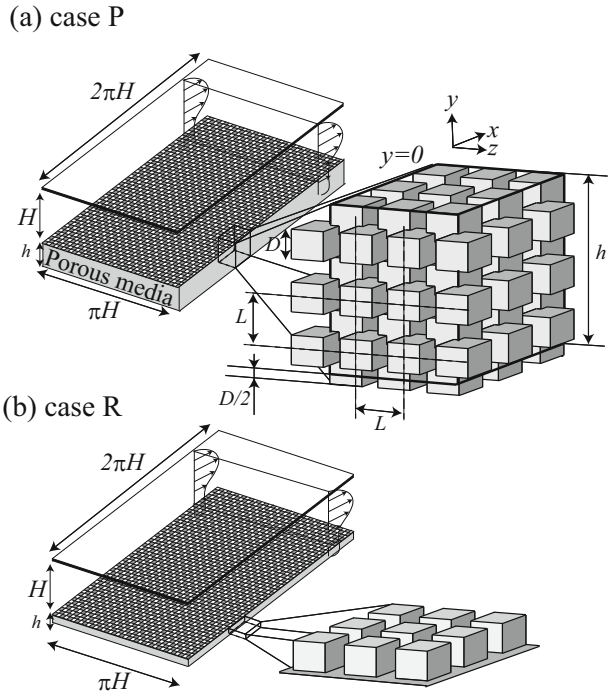

Fig. 1 Channel flow computational geometries: **a** case P, **b** case R

considered porous medium consisted of interconnected staggered cube arrays. The porosity φ, the permeability K and the other configuration parameters (cube size D and the cube pitch L) in the homogeneous region are summarised in Table 4. Since flows over porous media are principally affected by two factors which are the wall roughness and the wall permeability, two cases are simulated to investigate the influence of the wall permeability. They are namely case P: the simulation with the porous layer, and case R: the simulation with the rough wall that is shown in Fig. 1b. In those two cases, the surface structures were the same although the bottom wall thickness h was different. In case P, h was set as $h = 0.54H$ where H was the clear channel height, whilst in case R, it was set as $h = 0.088H$ which meant only one cube row was placed on the very bottom wall. Each computational domain size was $6.7H(x) \times (H+h)(y) \times 3.2H(z)$. Using the imbalance-correction grid-refinement

Table 4 Parameters of computational geometries

Case	φ	K/H^2	D/H	L/H	h/H	Grid node number ($x \times y \times z$)	Grid resolution	
P	0.71	1.7×10^{-4}	0.088	0.16	0.54	Fine($1674 \times 210 \times 837$)	$\Delta^{f+} = 1.2$,	$D/\Delta^f = 23$
						Coarse($837 \times 100 \times 419$)	$\Delta^{c,t+} = 1.6$	
R	–	–	0.088	0.16	0.088	Fine($1674 \times 89 \times 837$)	$\Delta^{f+} = 1.0$,	$D/\Delta^f = 23$
						Coarse($837 \times 100 \times 419$)	$\Delta^{c,t+} = 1.5$	

Table 5 Flow conditions of the simulation

Case	Re_b	Re_K	Re_τ	Re_τ^t	δ/H	C_f	C_f^t
P	2930	3.8	223	67	0.31	2.5×10^{-2}	1.1×10^{-2}
R	2920	0	161	76	0.37	1.6×10^{-2}	9.8×10^{-3}

method [14], the computational domain was decomposed into the finer and coarser resolution domains. Note that this method removes discontinuity problems of the higher order moments at the grid interface. The finer mesh domain covered near wall regions whilst the coarser mesh domain covered the core flow region of the clear channel. The grid node numbers and resolutions of the finer and coarser mesh regions are listed in Table 4. Not that the values with the superscripts "$t+$" and "$+$" indicate the values normalized by the friction velocities u_τ^t and u_τ, respectively. The friction velocity of the top smooth wall u_τ^t can be directly computed whilst the friction velocity of the bottom (porous or rough) wall u_τ is calculated by the balance between the pressure drop ΔP and the averaged wall shear stresses on the bottom and top walls as

$$(\tau_w + \tau_w^t) L_x L_z = L_y L_z \Delta P, \tag{6}$$

where $\tau_w = \rho(u_\tau)^2$ and $\tau_w^t = \rho(u_\tau^t)^2$. Thus, u_τ is given as

$$u_\tau = \left\{ -(u_\tau^t)^2 + \frac{\Delta P L_y}{\rho L_x} \right\}^{0.5}. \tag{7}$$

The grid resolution was confirmed to be fine enough by comparison with the results by a mesh of 1.5 times finer in each direction. Indeed, almost identical profiles of the flow variables were obtained by the two different meshes. Periodic boundary conditions were applied to the streamwise and spanwise directions with a constant streamwise pressure difference. For non-slip boundaries, which were applied to the surfaces of the top wall and the elements of the porous medium, the half-way bounce-back method was used whilst the slip boundary condition was imposed on the very bottom face of the domain in case P. The bulk Reynolds number was $\mathrm{Re}_b = U_b H/\nu \approx 3000$, the values of the permeability Reynolds number $\mathrm{Re}_K = u_\tau \sqrt{K}/\nu$, the friction Reynolds numbers on the solid and bottom walls $\mathrm{Re}_\tau^t = u_\tau^t \delta^t/\nu$ and $\mathrm{Re}_\tau = u_\tau \delta/\nu$ are listed in Table 5. Here, δ^t and δ are the distances from

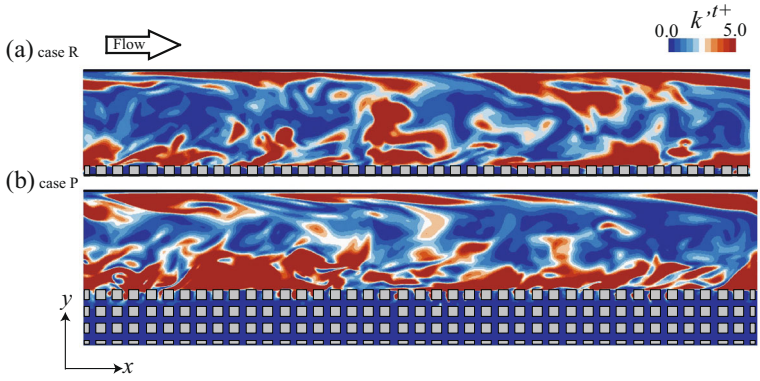

Fig. 2 Instantaneous turbulent kinetic energy distributions: **a** case R, **b** case P

the solid and bottom walls to the location where the Reynolds shear stress becomes zero: $\delta^t/H = (u_\tau^t)^2/[(u_\tau^t)^2 + (u_\tau)^2]$ and $\delta/H = (u_\tau)^2/[(u_\tau^t)^2 + (u_\tau)^2]$, respectively.

4 Results and Discussions

4.1 Instantaneous flow field

To capture general characteristics of the overall flow field, some instantaneous snapshots are displayed. Figure 2 shows instantaneous turbulent kinetic energy $k'[\equiv (u'^2 + v'^2 + w'^2)/2]$ contours in x-y planes. In Fig. 2a, there is no distinct difference between the levels of k'^{t+} over the rough and top smooth walls whilst stronger k'^{t+} is observed over the porous layer in Fig. 2b. It is seen that the generated turbulence over the porous layer is mostly transported

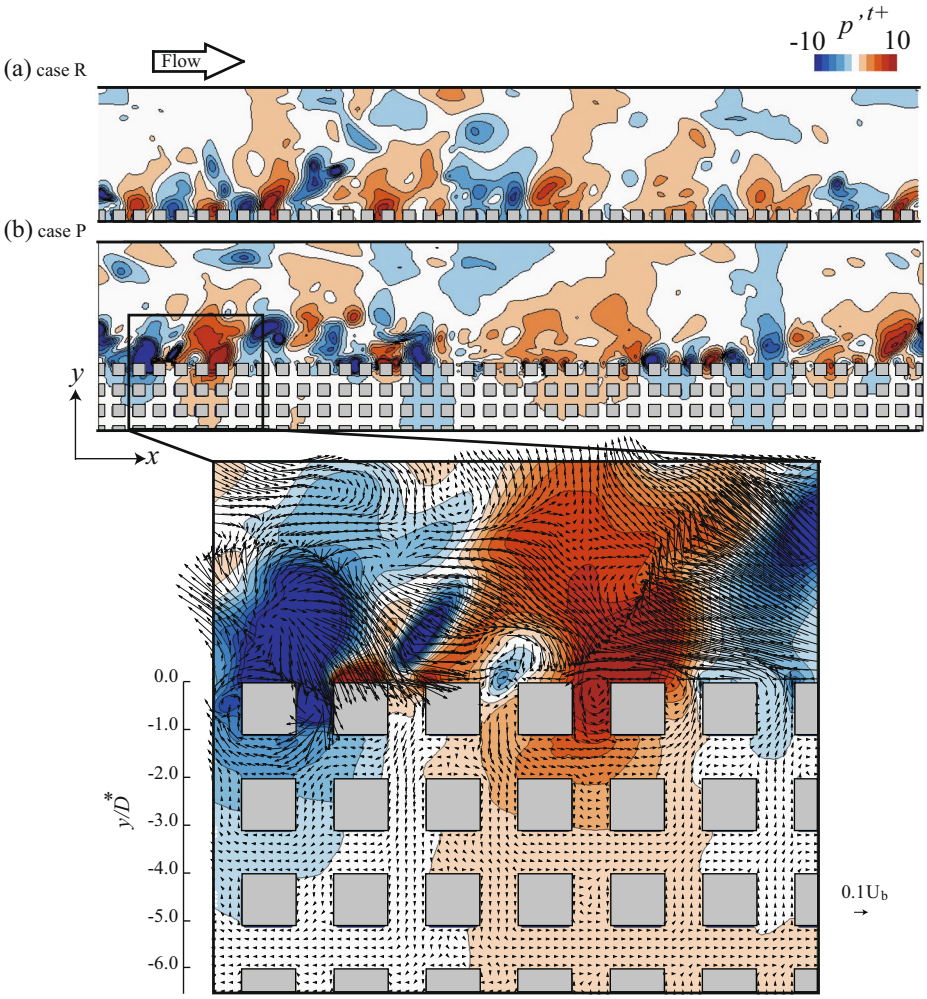

Fig. 3 Instantaneous pressure fields: **a** case R, **b** case P

to the clear channel region whilst the remaining part is rapidly dissipated inside the porous layer. It is not sustained deeply inside the porous layer.

Instantaneous pressure fields are shown in Fig. 3. Pressure fluctuations become significant over the rough and porous walls, which are induced by the K-H instability as reported by the previous study [15]. It should be noted that flows over highly permeable walls are known to behave as perturbed mixing layer flows rather than boundary layer flows and the inflection point of the streamwise velocity causes the K-H instability [7, 22, 24]. The instability becomes dominant when the shear penetration becomes large [17]. Interestingly, as shown in Fig. 3b, strong pressure fluctuations over the porous wall propagate deeply inside the porous layer as well as to the clear channel region. The velocity vectors zoomed up in Fig. 3b indicate that near the interface region the flows frequently go into and out from the porous layer and moderate velocity perturbations are induced underneath the interface of $-0.2 < y/D^* < 0$. However, velocity fluctuations are hardly observed deeply inside the porous layer at $y/D^* < -0.2$. Here, D^* indicates a half of the cube pitch: $D^* = L/2$. In the same flow geometries, our previous report [15] discussed on the presence and the size of large scale spanwise rolls induced by the K-H instability through the two-point correlation and the proper orthogonal decomposition. It was reported that the wavelength of 550 wall units estimated by the two-point correlation corresponded to the most energy containing motions.

4.2 Turbulence statistics

For discussing turbulence statistically, plane averaging of a variable $\phi(x, y, z)$ is defined as

$$[\phi(y)]^f = \frac{1}{A_{S_f}} \int_S \phi(x, y, z) dS, \tag{8}$$

where S and A_{S_f} are the surface of a x-z plane and the surface areas of the fluid phase contained within S, respectively. Following the derivation of the volume averaged momentum equation by Whitaker [29], the plane and Reynolds averaged (double averaged) momentum equation can be derived as

$$\begin{aligned}
\frac{\partial [\overline{u_i}]^f}{\partial t} + \left[\overline{u_j}\right]^f \frac{\partial [\overline{u_i}]^f}{\partial x_j} = &- \frac{1}{\rho} \frac{\partial [\overline{p}]^f}{\partial x_i} + \frac{\partial}{\partial x_j} \left(\nu \frac{\partial [\overline{u_i}]^f}{\partial x_j} \right) \\
&- \frac{\partial}{\psi \partial x_j} \psi \left(\underbrace{\left[\overline{u_i' u_j'}\right]^f}_{R_{ij}} + \underbrace{\left[\tilde{\overline{u}}_i \tilde{\overline{u}}_j\right]^f}_{\mathcal{T}_{ij}} \right) \\
&- \underbrace{\left(\frac{1}{\psi \rho A_S} \int_\ell n_i \tilde{\overline{p}} d\ell - \frac{\nu}{\psi A_S} \int_\ell n_j \frac{\partial \tilde{\overline{u}}_i}{\partial x_j} d\ell \right)}_{f_i} \\
&+ \underbrace{\frac{\nu}{\psi} \left(\frac{\partial \psi}{\partial x_j} \frac{\partial [\overline{u}_i]^f}{\partial x_j} + [\overline{u}_i]^f \frac{\partial^2 \psi}{\partial x_j^2} \right)}_{g_i^\psi},
\end{aligned} \tag{9}$$

where ℓ is the total length of the solid obstacle within an averaging surface and n_k is its unit normal vector pointing outward from the fluid to solid phases. The surface porosity ψ is defined as $\psi = A_S/A_{S_f}$. Here, A_S is the surface area of the x-z plane. The second moments

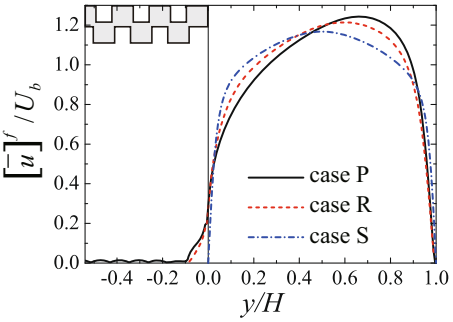

Fig. 4 Plane averaged streamwise mean velocity profiles

R_{ij} and $\mathcal{T}_{ij}$ are the plane averaged Reynolds stress and the plane-dispersive covariance (dispersive stress), respectively. The terms f_i and g_i^{ψ} are, respectively, the drag force term and the hetero porous term arising from the inhomogeneity of the surface porosity. To obtain the statistical quantities, averaging over 4×10^5 time steps is carried out. The time duration corresponds to 25 turn-over-times. The quantities including gradients are obtained by the fourth-order central difference.

Figures 4 and 5 show the plane averaged streamwise mean velocity and the off-diagonal components R_{12}^{t+} and $\mathcal{T}_{12}^{t+}$ normalised by u_τ^t, respectively. For comparison with those over a smooth wall (case S), the DNS data of Kim et al. [11] at $\mathrm{Re}_\tau = 180$ are also plotted. Note that the friction Reynolds numbers of the cases are in the same level. (In cases P and R, $\mathrm{Re}_\tau = 223$ and $\mathrm{Re}_\tau = 161$, respectively). Figure 5 shows that R_{12}^{t+} over the bottom wall is significantly enhanced in cases P and R whereas $\mathcal{T}_{12}^{t+}$ is negligibly small compared with R_{12}^{t+}. This means that the contribution of $\mathcal{T}_{12}^{t+}$ to the streamwise mean velocity is far smaller than that of R_{12}^{t+}. The enhancement of R_{12}^{t+} is more significant in case P than in case R and it makes the streamwise mean velocity profile skewed as seen in Fig. 4. Corresponding to the enhancement of the plane averaged Reynolds shear stress, the friction factor $C_f = 2(u_\tau / U_b)^2$ of the rough wall is 1.4 times as high as that of the top smooth wall: C_f^t, whilst C_f of the porous wall is 2.3 times as high as C_f^t as shown in Table 5. Consequently, it is confirmed that both wall roughness and permeability enhance the friction factor.

On semi-logarithmic coordinates, Fig. 6 shows the velocity profiles defined as

$$[\overline{u}]^{f+} = \frac{1}{\kappa} ln \left\{ \frac{(y+d)^+}{h_r^+} \right\}, \tag{10}$$

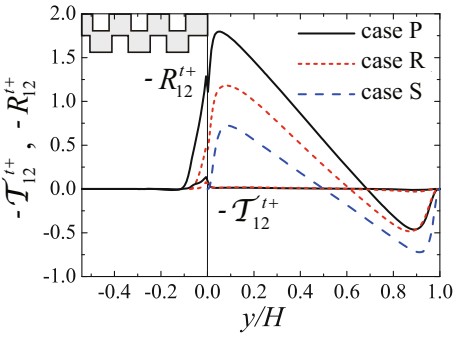

Fig. 5 Off-diagonal components of the second moments: R_{12}^{t+} and $\mathcal{T}_{12}^{t+}$

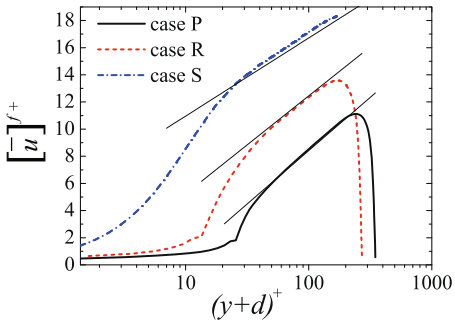

Fig. 6 Semi-logarithmic plots of the streamwise mean velocities

where parameters κ, d and h_r are, respectively, Kármán constant, the zero-plane displacement and the equivalent roughness height. As reported by our previous report [15], in which the vortex structure over the same flow geometries was discussed, κ of case P is smaller than that of case R whilst d and h_r of case P are significantly larger than those of case R. To compare them with those of the other studies, Fig. 7 indicates κ, h_r and d of case P with the DNS [2] and experimental [4, 17, 27] data. With the increase of the permeability Reynolds number Re_K, κ tends to decrease (Fig. 7a) whereas h_r and d tend to increase (Fig. 7b, c) as in Refs. [17, 27]. It is seen that the present results well accord with the experimental data of Suga et al. [27] for porous-walled channel flows.

In order to investigate the contribution of quadrant events to the plane averaged Reynolds shear stress, Fig. 8 shows the plane averaged Reynolds shear stress decomposed into the first quadrant (Q_1): outward interactions, the second quadrant (Q_2): ejections, the third quadrant (Q_3): inward interactions and the fourth quadrant (Q_4): sweeps. At the interface, Q_2 and Q_4 motions become larger in case P than those in case R. The sweep and ejection events over the porous layer seem to be associated with large scale pressure fluctuations as observed in the instantaneous velocity vectors of Fig. 3b. (See [15] for detailed discussions on this large scale motion). Although Q_4 motions are most dominant at the interface in both cases, Q_2 motions overtake them at $y/H = 0.040$ ($y^+ = 13$) in case P and at $y/H = 0.048$ ($y^+ = 13$) in case R. This trend is the same as that seen in the experimental studies [7, 25, 28]. From the probability density of the quadrant events $P(Q_i)$ shown in Fig. 9, it is understood that the ejections occur more frequently than the sweeps though the contribution of the sweeps is more dominant inside the bottom wall at $-1.0 < y/D^* < 0$ as seen in Fig. 8. Such a tendency is more obvious in case P. This implies that weak ejections are most dominant inside the porous layer whilst less frequent but stronger sweeps contribute more to the shear stress generation. This supports the discussion of Ref. [23].

Figure 10 shows profiles of the plane averaged turbulent kinetic energy $k(\equiv R_{kk}/2)$. The profiles normalised by u_τ^t show local maxima and are significantly enhanced over the bottom wall in cases P and R. The enhancement is more significant over the porous layer. Figure 11 shows k and $\mathcal{K}(\equiv \mathcal{T}_{kk}/2)$ distributions normalised by the friction velocity on the bottom wall u_τ. In Fig. 11a, it is found that k^+ over the porous layer becomes lower than those over the rough and smooth walls. This is because the wall shear stress over the porous wall is more significantly enhanced than the turbulent kinetic energy. Figure 11a also shows that k^+ inside the porous layer becomes larger and its penetration is deeper than that in the rough wall. The penetration of k^+ inside the porous layer reaches to $y/D^* = -2.0$. As seen in Fig. 11b, the levels of $\mathcal{K}^+$ in cases P and R are roughly the same at $y/H < 0$.

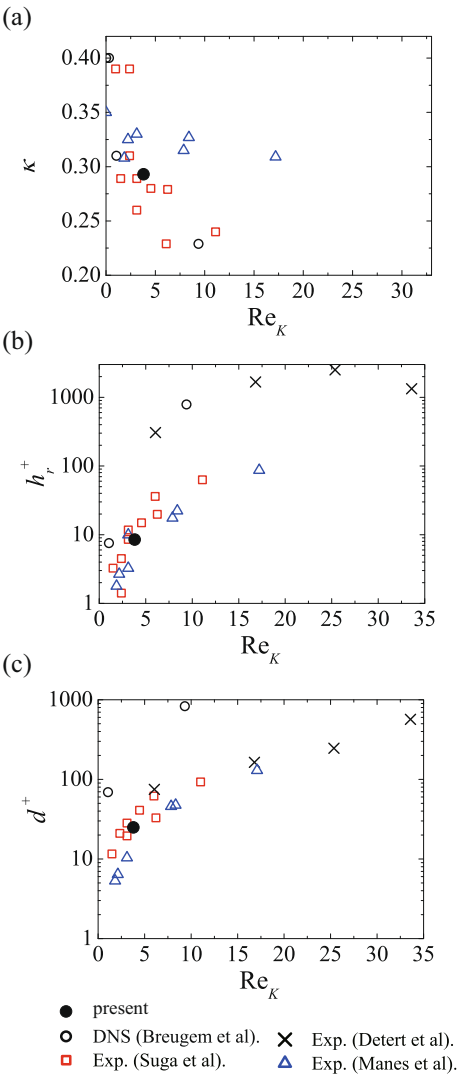

Fig. 7 Comparison of the parameters for the mean velocity profiles over porous layers: **a** Kármán constant κ, **b** equivalent roughness height h_r, **c** zero-plane displacement d

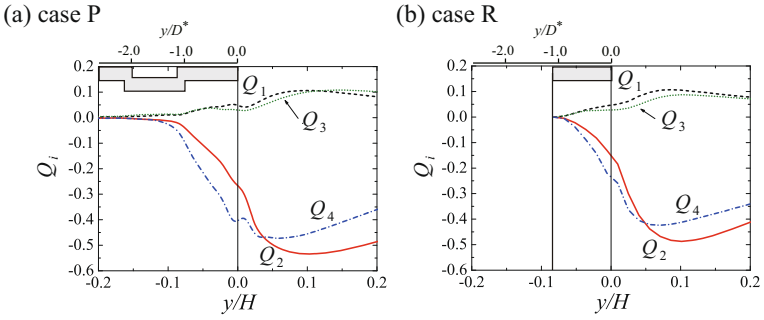

Fig. 8 Quadrant analysis of the plane averaged Reynolds shear stress: **a** case P, **b** case R

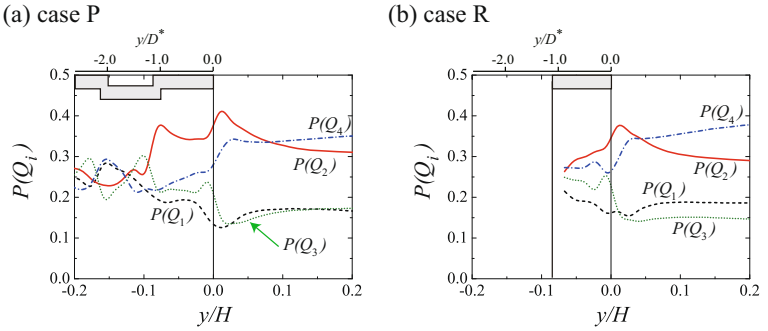

Fig. 9 Probability density of the quadrant events: **a** case P, **b** case R

Figure 12 presents the plane averaged Reynolds stress and the plane-dispersive covariance over and inside the bottom wall. In Fig. 12a, it is seen that R_{11}^+ over the bottom wall ($y/H > 0$) becomes smaller in case P whilst R_{22}^+ and R_{33}^+ become larger compared with those of case R. This indicates that turbulence becomes more isotropic in case P than in case R. In case P, although the plane averaged Reynolds stress components become $R_{11}^+ > R_{33}^+ > R_{22}^+$ over the porous layer ($y/H > 0$), the streamwise and spanwise components: R_{11}^+ and R_{33}^+, rapidly decay inside the porous layer and the relation becomes $R_{22}^+ > R_{11}^+ > R_{33}^+$ in the region of $-2.2 < y/D^* < -1.0$. It is also found that R_{12}^+ in case P is larger and is more rapidly damped than the normal stresses. This tendency was also seen in Ref. [2]. Moreover, in the present results, it is seen that the profiles of R_{11}^+ and R_{33}^+ are affected by the solid elements whilst, interestingly, such a structural effect on R_{22}^+ and R_{12}^+ is not obvious. Indeed, the profiles of R_{22}^+ and R_{12}^+ do not show clearly the wavy shapes corresponding to the structure. As seen in Fig. 12b, although $\mathcal{T}_{12}^+$ is hardly produced in both cases, the normal components $\mathcal{T}_{ii}$ are produced inside the bottom wall. The distributions of the streamwise component $\mathcal{T}_{11}^+$ in both cases show similar profiles underneath the interface of $-1.0 < y/D^* < 0.0$ and the levels are the same as that of R_{11}^+ whereas $\mathcal{T}_{22}^+$ and $\mathcal{T}_{33}^+$ are far smaller than $\mathcal{T}_{11}^+$. Deeply inside the porous layer at $y/D^* < -2.0$, only the streamwise

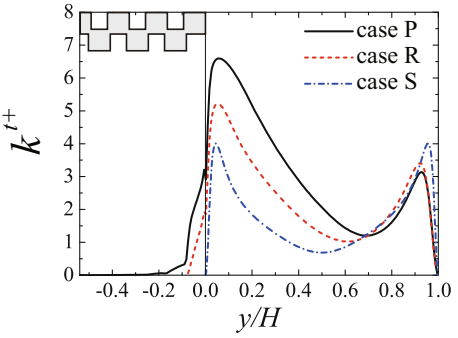

Fig. 10 Plane averaged turbulent kinetic energy profiles normalised by the top-wall friction velocity

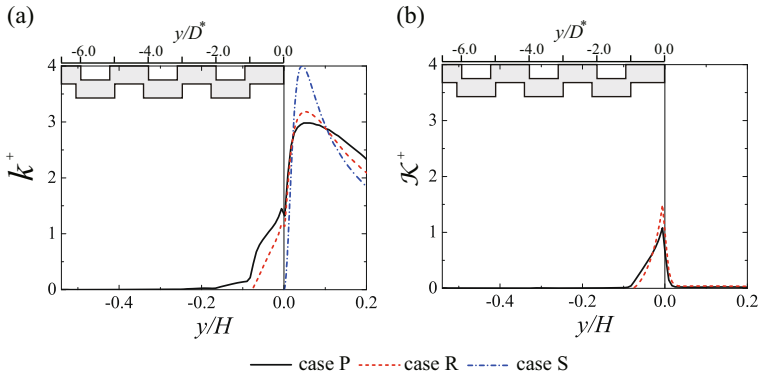

Fig. 11 Plane averaged turbulent kinetic energy and the plane-dispersion energy profiles normalised by the bottom-wall friction velocity: **a** plane averaged turbulent kinetic energy k^+, **b** plane-dispersion energy $\mathcal{K}^+$

component $\mathcal{T}_{11}^+$ exists and the other components are hardly observed. The fact of $\mathcal{T}_{12} \simeq 0$ despite the existence of the mean shear under the bottom wall indicates that the usual eddy viscosity form for $\mathcal{T}_{ij}$ cannot be valid for turbulence modelling.

Figure 13 shows the plane averaged pressure fluctuation. Although k^+ over the porous layer becomes lower than those over the rough and smooth walls as seen in Fig. 11a, the plane averaged pressure fluctuation of case P surpasses those of cases R and S. It is because of significant pressure perturbations by the K-H instability over the porous layer and the substantial pressure fluctuation is sustained deeply inside the porous layer.

4.3 Budget term analysis

To discuss the turbulent transport, the plane averaged transport equation of the Reynolds stress $\overline{u_i'u_j'}$ is derived as

$$\left[\frac{\partial \overline{u_i'u_j'}}{\partial t}\right]^f + \left[\overline{u}_k \frac{\partial \overline{u_i'u_j'}}{\partial x_k}\right]^f = \underbrace{\left[-\frac{\partial \overline{u_i'u_j'u_k'}}{\partial x_k}\right]^f}_{D_{ij}^t} \underbrace{-\frac{1}{\rho}\left[\frac{\partial \overline{u_i'p'}}{\partial x_j} + \frac{\partial \overline{u_j'p'}}{\partial x_i}\right]^f}_{D_{ij}^p}$$
$$+ \underbrace{\left[\frac{\partial}{\partial x_k}\left(\nu \frac{\partial \overline{u_i'u_j'}}{\partial x_k}\right)\right]^f}_{D_{ij}^\nu} + \underbrace{\left[\overline{\frac{p'}{\rho}\left(\frac{\partial u_i'}{\partial x_j} + \frac{\partial u_j'}{\partial x_i}\right)}\right]^f}_{\phi_{ij}}$$
$$- \underbrace{\left[\overline{u_i'u_k'}\frac{\partial \overline{u_j}}{\partial x_k} + \overline{u_j'u_k'}\frac{\partial \overline{u_i}}{\partial x_k}\right]^f}_{P_{ij}} \underbrace{- 2\nu\left[\overline{\frac{\partial u_i'}{\partial x_k}\frac{\partial u_j'}{\partial x_k}}\right]^f}_{\varepsilon_{ij}}, \quad (11)$$

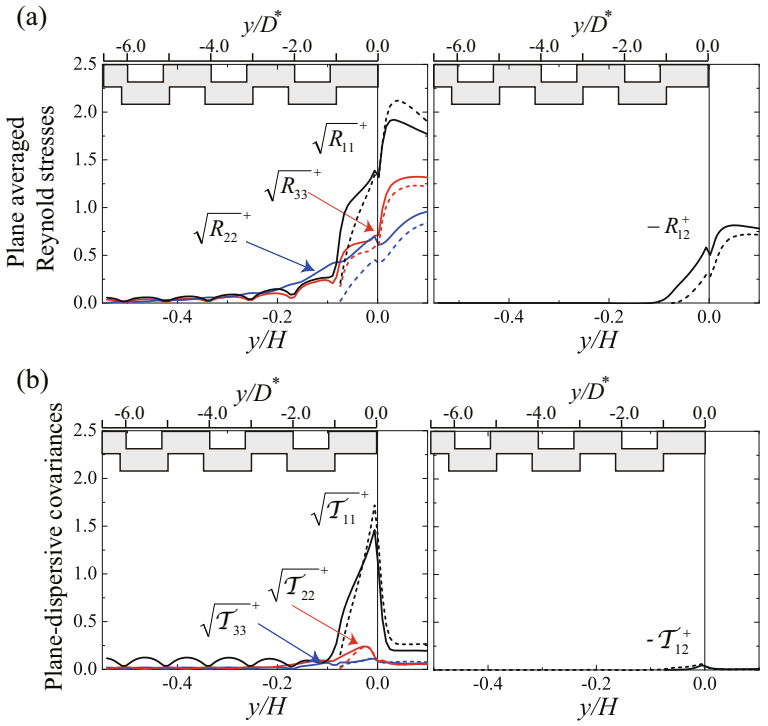

Fig. 12 Plane averaged second moment profiles around the bottom wall: **a** plane averaged Reynolds stress R_{ij}^+, **b** plane-dispersive covariance $\mathcal{T}_{ij}^+$; *solid lines*: case P, *dashed lines*: case R

where D_{ij}^t, D_{ij}^p ,D_{ij}^v, ϕ_{ij}, P_{ij} and ε_{ij} are the turbulent, pressure and viscous diffusions, re-distribution, production and dissipation terms, respectively. The second term in the left-hand side of Eq. 11 can be decomposed as

$$\left[\overline{u_k}\frac{\partial \overline{u_i'u_j'}}{\partial x_k}\right]^f = [\overline{u_k}]^f \frac{\partial \left[\overline{u_i'u_j'}\right]^f}{\partial x_k} + \underbrace{\left[\tilde{\overline{u}}_k \frac{\partial \overline{u_i'u_j'}}{\partial x_k}\right]^f}_{-T_{ij}^d}, \tag{12}$$

where T_{ij}^d expresses the turbulent transport by dispersion. Hence, Eq. 11 may be rewritten symbolically as

$$\frac{\partial R_{ij}}{\partial t} + [\overline{u_k}]^f \frac{\partial R_{ij}}{\partial x_k} = T_{ij}^d + D_{ij}^t + D_{ij}^p + D_{ij}^v + \phi_{ij} + P_{ij} - \varepsilon_{ij}. \tag{13}$$

Figure 14 shows the profiles of the budget terms of Eq. 13 for R_{11}^+. The turbulent production is found to be maximum over the porous and rough walls. The production of case R becomes larger than that of case P over the bottom wall whilst, inside the bottom wall, P_{11}^+ of case P exceeds that of case R. However, the penetration of P_{11}^+ in case P is limited in the region of $-1.3 < y/D^*$. Over the bottom wall, the level of P_{11}^+ in case P is smaller than that in case R although the levels of ϕ_{11}^+ are roughly the same. It means that the ratio of ϕ_{11}^+/P_{11}^+ of case P is larger and this makes turbulence more isotropic as shown in Fig. 12a.

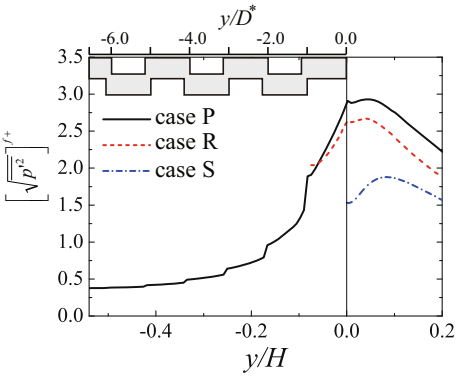

Fig. 13 Plane averaged pressure fluctuation profiles

The enhanced re-distribution is associated with the pressure fluctuation induced and intensified by the K-H instability as shown in Fig. 13. In both cases, although T_{11}^{d+} is negligible, the dissipation term ε_{11}^{+} and the viscous diffusion term $D_{11}^{\nu+}$ show pointed peaks near the edges of the solid elements at $y/D^* = 0.0, -1.0$. The turbulent diffusion D_{11}^{t+} works as a sink term over the bottom wall but it works as a source term inside the bottom wall near $y/D^* = -1.0$. This means that D_{11}^{t+} transports the energy into the bottom wall whereas the diffusion by $D_{11}^{\nu+}$ is limited near the edges of the solid elements.

Figure 15 compares the profiles of the budget terms of the R_{22}^{+} equation. Although both profiles of ϕ_{22}^{+} over the bottom walls are similar, they are different inside the walls. In case P, ϕ_{22}^{+} works as a source in the region of $-0.9 < y/D^* < 0.0$ and its effect is more significant

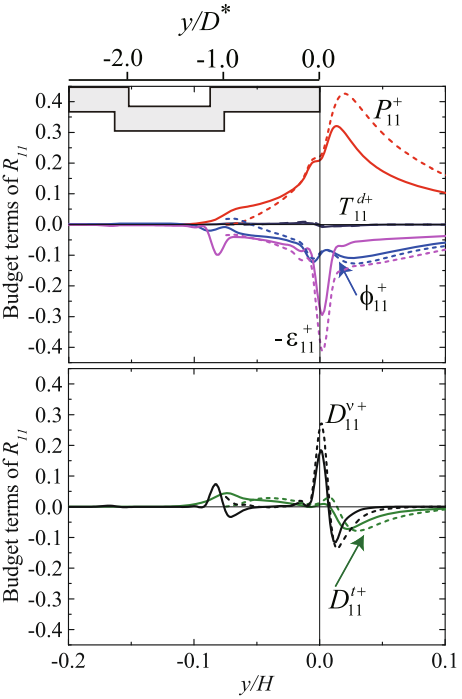

Fig. 14 Budget terms of the transport equation of R_{11}^{+}; *solid lines*: case P, *dashed lines*: case R

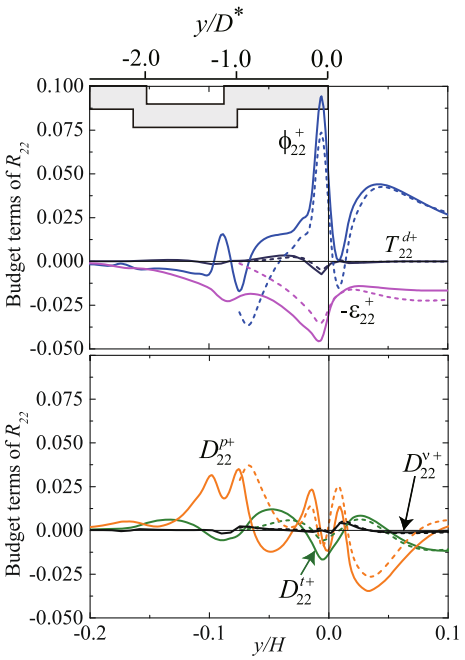

Fig. 15 Budget terms of the transport equation of R_{22}^{+}; *solid lines*: case P, *dashed lines*: case R

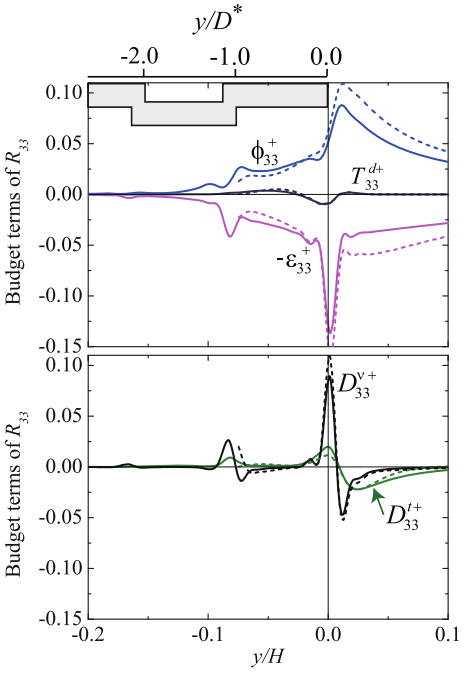

Fig. 16 Budget terms of the transport equation of R_{33}^{+}; *solid lines*: case P, *dashed lines*: case R

than in case R. In the region of $y/D^* < -1.4$, ϕ_{22}^+ of case P becomes negative and thus the energy of R_{22}^+ is transported to the other components. The viscous diffusion term $D_{22}^{\nu+}$ and the dispersion transport term T_{22}^{d+} of both cases are small whilst the pressure and turbulent diffusion terms: D_{22}^{t+} and D_{22}^{p+}, are substantially large. In case P, D_{22}^{t+} gains energy in $-0.9 < y/D^* < -0.3$ whilst D_{22}^{p+} gains energy more deeply inside the porous layer of $y/D^* < -0.9$. It is confirmed that the processes of ϕ_{22}^+ and D_{22}^{p+} play very important roles deeply inside the porous layer and this supports the results of Ref. [2]. This is due to the strong pressure fluctuation sustained inside the porous layer as shown in Fig. 13. Unlike in the streamwise component, $D_{22}^{\nu+}$ and ε_{22}^+ do not show sharp peaks at the interface. Its reason is that because of the limiting behaviour of the wall-normal velocity component toward a wall, dv/dy becomes small in the vicinity of the wall leading to the insignificant profiles of $D_{22}^{\nu+}$ and ε_{22}^+.

Figure 16 shows the profiles of the budget terms of the R_{33}^+ equation. The profiles of the re-distribution term ϕ_{33}^+ have local maxima over the porous and rough walls. The profile of ϕ_{33}^+ in case P is smaller than that in case R over the interface while it becomes larger than that in case R inside the bottom wall. The viscous diffusion term $D_{33}^{\nu+}$ has peaks near $y/D^* = 0.0, -1.0$ in both cases and the processes of D_{33}^{t+} and T_{33}^{d+} become negligibly small inside the walls. It is noticed that, inside the porous layer, ϕ_{33}^+ is still dominant and works as a counter part of ε_{33}^+.

Figure 17 shows the distributions of the budget terms of the R_{12}^+ equation. It is found that the main processes are ϕ_{12}^+, D_{12}^{p+} and P_{12}^+ and the other processes are negligible. The magnitudes of ϕ_{12}^+ and D_{12}^{p+} become significant near $y/D^* = 0.0, -1.0$ and they seem to

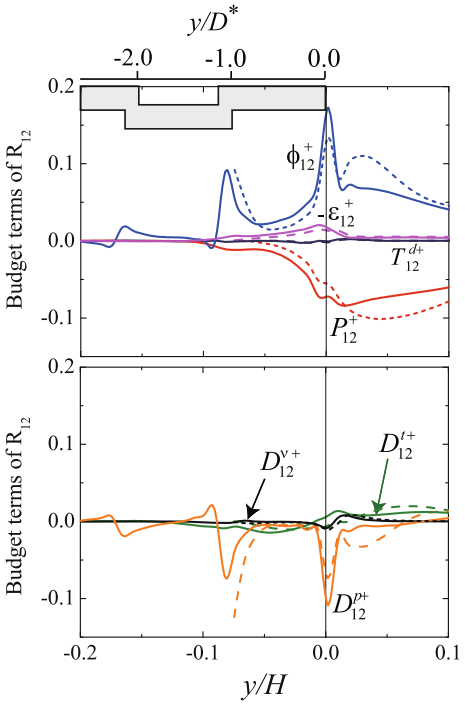

Fig. 17 Budget terms of the transport equation of R_{12}^+; *solid lines*: case P, *dashed lines*: case R

work as the counter processes to each other. Indeed, in the region of $y/D^* < -1.0$, they almost balance each other out ($D_{12}^{p+} + \phi_{12}^{+} \approx 0$). Furthermore, P_{12}^{+} of case P becomes larger than that of case R inside the bottom wall and it rapidly decays to zero in the region of $y/D^* < -1.0$. This is the reason why R_{12}^{+} rapidly decays inside the porous layer as shown in Fig. 12a.

To discuss the mutual dependency between turbulence and dispersion, transport equations of the plane averaged turbulent kinetic energy and the plane-dispersion energy are considered. Their transport equations are symbolically written as

$$\frac{Dk}{Dt} = D_k + P_k^s + P_k^d - \varepsilon, \tag{14}$$

$$\frac{D\mathcal{K}}{Dt} = D_{\mathcal{K}} + P_{\mathcal{K}}^s - P_k^d + \mathcal{F} - \mathcal{E}, \tag{15}$$

where D_k and ε are the diffusion and dissipation terms of k, and $D_{\mathcal{K}}$ and $\mathcal{E}$ are the diffusion and dissipation terms of $\mathcal{K}$, respectively. (See Kuwata and Suga [12], for the detailed derivation of Eq. 15). The term $\mathcal{F}(\equiv \overline{f}_i\,[\overline{u_i}]^f)$ is the drag force term. The production terms P_k^s and P_k^d in Eq. 14 are the mean shear production and the mean dispersive-shear production terms, respectively. They are obtained by the decomposition of the production term

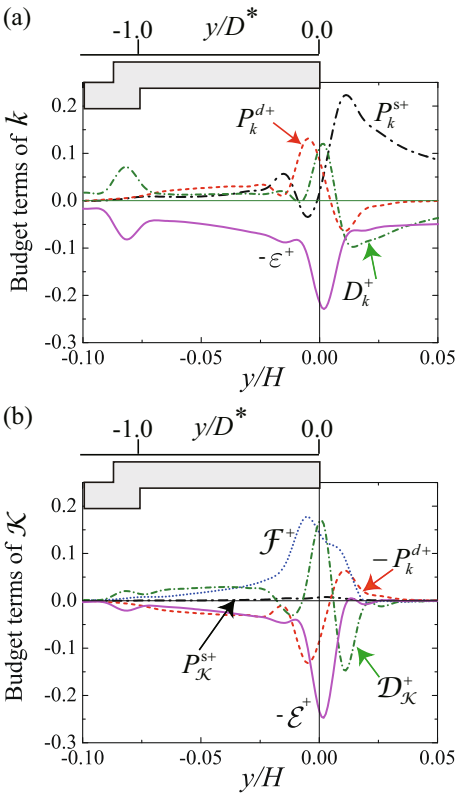

Fig. 18 Budget terms of the transport equations of k^+ and $\mathcal{K}^+$ for case P: **a** budget terms of k^+, **b** budget terms of $\mathcal{K}^+$

$P_{kk}/2$ in Eq. 13. The production $P^s_{\mathcal{K}}$ in Eq. 15 is the mean shear production for $\mathcal{K}$. They are expressed as

$$P^s_k = -R_{ik}\frac{\partial\,[\overline{u}_i]^f}{\partial x_k}, \quad P^s_{\mathcal{K}} = -\mathcal{T}_{ik}\frac{\partial\,[\overline{u}_i]^f}{\partial x_k}, \quad P^d_k = -\left[\overline{\tilde{u}'_i\tilde{u}'_k}\frac{\partial\tilde{\overline{u}}_i}{\partial x_k}\right]^f. \tag{16}$$

It is noted that P^d_k appears with positive sign in Eq. 14 whilst it appears with negative sign in Eq. 15. This indicates that P^d_k exchanges energy between k and $\mathcal{K}$.

Figure 18 compares the budget terms of Eqs. 14 and 15. Figure 18a shows that the mean shear production P^s_k becomes dominant and the mean dispersive-shear production P^d_k works as a sink term over the porous layer whereas, inside the porous layer, P^d_k becomes a dominant source term. The turbulence generation by P^s_k and P^d_k vanishes in the region of $y/D^* < -1.0$, and the diffusion process of D_k transports the energy to that region. Although P^s_k is the main source term for k over the porous layer, Fig. 18b shows that $P^s_{\mathcal{K}}$ of $\mathcal{K}$ hardly produces energy and the drag force term $\mathcal{F}$ is found to be the main source term instead of $P^s_{\mathcal{K}}$. Inside the porous layer, $(-P^d_k)$ becomes negative and its sink effect is nearly the same as that by the dissipation. This means that the gained energy by $\mathcal{F}$ is transferred from $\mathcal{K}$ to k by P^d_k and it becomes the main source for k inside the porous layer. Inside the porous layer of $y/D^* < -0.4$, although the diffusion term $D_{\mathcal{K}}$ exceeds $\mathcal{F}$, it transports energy less than D_k of k. This is the reason why $\mathcal{K}$ decays more rapidly than k inside the porous layer as shown in Fig. 11. These results imply that for predicting k precisely, it is necessary to model P^d_k and D_k properly inside the porous layer of $-0.075 < y/H < 0$ and $y/H < -0.075$, respectively. As seen in Fig. 18b, since $P^s_{\mathcal{K}}$ hardly contributes to generate the dispersion energy $\mathcal{K}$ but $\mathcal{F}$ is the main source inside the porous layer, one can correlate $\mathcal{K}$ and $\mathcal{F}$ as reported by Kuwata snd Suga [16].

5 Conclusions

Studies on the turbulent transport of interface turbulence over the porous and rough walls are carried out using the DNS data of porous- and rough-walled channel flows at a bulk Reynolds number 3000. The considered porous medium consists of interconnected staggered cube arrays with a porosity of 0.71 and the rough wall has the same surface structure. By the quadrant and budget term analyses, the turbulent transport mechanisms around porous and rough walls are discussed in detail. The key findings in the present study are:

(1) Although weak ejections become dominant near the porous and rough walls, less frequent but more energetic sweeps contribute more to the plane averaged Reynolds shear stress. This trend is more remarkable over the porous layer.
(2) Near the porous and rough walls, the off-diagonal components of the plane-dispersive covariance are hardly produced whilst the normal components are produced inside the walls. Compared with the plane averaged Reynolds stresses, the levels of the wall-normal and spanwise components are far smaller though the streamwise component keeps the same level.
(3) The pressure perturbations induced and intensified by the K-H instability over the porous layer strengthen the re-distribution and pressure diffusion processes. The significant re-distribution makes turbulence more isotropic over the porous layer. The intensified pressure diffusion carries the wall-normal component of the plane averaged Reynolds stress deeply inside the porous layer. However, since the pressure diffusion

and the re-distribution for the plane averaged Reynolds shear stress balance each other out inside the porous layer, the plane averaged Reynolds shear stress rapidly decays unlike the normal components.

(4) For the plane averaged turbulent kinetic energy, the mean shear production is the main source over the porous layer and the mean dispersive-shear production, which transports the energy from the plane-dispersion energy, becomes dominant inside the porous layer.

(5) For the plane-dispersion energy, the drag force is the main energy source instead of the mean shear production inside the porous layer and the gained energy is partly transferred to the plane averaged turbulent kinetic energy by the mean dispersive-shear production. The magnitudes of this energy transport and the dissipation are comparable.

Acknowledgments The authors express their gratitude to Dr. M Kaneda for his support. A part of this study was financially supported by the research grants (No.26·10154) of the JSPS Japan. The numerical calculations were carried out on TSUBAME 2.5 supercomputer in Tokyo Institute of Technology.

References

1. Breugem, W.P., Boersma, B.J.: Direct numerical simulations of turbulent flow over a permeable wall using a direct and a continuum approach. Phys. Fluids **17**, 025103 (2005)
2. Breugem, W.P., Boersma, B.J., Uittenbogaard, R.E.: The influence of wall permeability on turbulent channel flow. J. Fluid Mech. **562**, 35–72 (2006)
3. Chandesris, M., D'Hueppe, A., Mathieu, B., Jamet, D., Goyeau, B.: Direct numerical simulation of turbulent heat transfer in a fluid-porous domain. Phys. Fluids **25**(12), 125110 (2013)
4. Detert, M., Nikora, V., Jirka, G.H.: Synoptic velocity and pressure fields at the water–sediment interface of streambeds. J. Fluid Mech. **660**, 55–86 (2010)
5. d'Humiéres, D., Ginzburg, I., Krafczyk, M., Lallemand, P., Luo, L.S.: Multiple-relaxation-time lattice Boltzmann models in three dimensions. Phil. Trans. R. Soc. A **360**, 437–451 (2002)
6. Dwyer, M.J., Patton, E.G., Shaw, R.H.: Turbulent kinetic energy budgets from a large-eddy simulation of airflow above and within a forest canopy. Boundary-Layer Meteorol. **84**(1), 23–43 (1997)
7. Finnigan, J.J., Shaw, R.H., Patton, E.G.: Turbulence structure above a vegetation canopy. J. Fluid Mech. **637**, 387–424 (2009)
8. He, X., Luo, L.S.: Lattice Boltzmann model for the incompressible Navier-Stokes equation. J. Stat. Phys. **88**(3-4), 927–944 (1997)
9. Kang, S.K., Hassan, Y.A.: The effect of lattice models within the lattice Boltzmann method in the simulation of wall-bounded turbulent flows. J. Comput. Phys. **232**(1), 100–117 (2013)
10. Katul, G.: An investigation of higher-order closure models for a forested canopy. Boundary-Layer Meteorol. **89**(1), 47–74 (1998)
11. Kim, J., Moin, P., Moser, R.: Turbulence statistics in fully developed channel flow at low Reynolds number. J. Fluid Mech. **177**, 133–166 (1987)
12. Kuwata, Y., Suga, K.: Modelling turbulence around and inside porous media based on the second moment closure. Int. J. Heat Fluid Flow **43**, 35–51 (2013)
13. Kuwata, Y., Suga, K.: Anomaly of the lattice Boltzmann methods in three-dimensional cylindrical flows. J. Comput. Phys. **280**, 563–569 (2015)
14. Kuwata, Y., Suga, K.: Imbalance-correction grid-refinement method for lattice Boltzmann flow simulations. J. Comput. Phys. **311**, 348–362 (2016)
15. Kuwata, Y., Suga, K.: Lattice Boltzmann direct numerical simulation of interface turbulence over porous and rough walls. Int. J. Heat Fluid Flow (2016). doi:10.1016/j.ijheatfluidflow.2016.03.006
16. Kuwata, Y., Suga, K., Sakurai, Y.: Development and application of a multi-scale $k-\varepsilon$ model for turbulent porous medium flows. Int. J. Heat Fluid Flow **49**, 135–150 (2014)
17. Manes, C., Poggi, D., Ridolfi, L.: Turbulent boundary layers over permeable walls: scaling and near-wall structure. J. Fluid Mech. **687**, 141–170 (2011)

18. Manes, C., Pokrajac, D., McEwan, I., Nikora, V.: Turbulence structure of open channel flows over permeable and impermeable beds a comparative study. Phys. Fluids **21**, 125109 (2009)
19. Meyers, T.P., Baldocchi, D.D.: The budgets of turbulent kinetic energy and Reynolds stress within and above a deciduous forest. Agric. For. Meteorol. **53**(3), 207–222 (1991)
20. Nepf, H.M.: Drag, turbulence, and diffusion in flow through emergent vegetation. Water Resour. Res. **35**(2), 479–489 (1999)
21. Nezu, I., Sanjou, M.: Turburence structure and coherent motion in vegetated canopy open-channel flows. J. Hydro-Environ. Res. **2**, 62–90 (2008)
22. Poggi, D., Porporato, A., Ridolfi, L., Albertson, J.D., Katul, G.G.: The effect of vegetation density on canopy sub-layer turbulence. Boundary-Layer Meteorol. **111**(3), 565–587 (2004)
23. Pokrajac, D., Manes, C.: Velocity measurements of a free-surface turbulent flow penetrating a porous medium composed of uniform-size spheres. Transp. Porous Med. **78**, 367–383 (2009)
24. Raupach, M.R., Finnigan, J.J., Brunei, Y.: Coherent eddies and turbulence in vegetation canopies: the mixing-layer analogy. Boundary-Layer Meteorol. **78**(3-4), 351–382 (1996)
25. Suga, K.: Understanding and modelling turbulence over and inside porous media. Flow Turbulence Combust. **96**, 717–756 (2016)
26. Suga, K., Kuwata, Y., Takashima, K., Chikasue, R.: A D3Q27 multiple-relaxation-time lattice Boltzmann method for turbulent flows. Comput. Math. Appl. **69**, 518–529 (2015)
27. Suga, K., Matsumura, Y., Ashitaka, Y., Tominaga, S., Kaneda, M.: Effects of wall permeability on turbulence. Int. J. Heat Fluid Flow **31**, 974–984 (2010)
28. Suga, K., Mori, M., Kaneda, M.: Vortex structure of turbulence over permeable walls. Int. J. Heat Fluid Flow **32**, 586–595 (2011)
29. Whitaker, S.: Flow in porous media I: A theoretical derivation of Darcy's law. Transp. Porous Med. **1**, 3–25 (1986)
30. Whitaker, S.: The Forchheimer equation: A theoretical development. Transp. Porous Med. **25**, 27–61 (1996)
31. White, A.T., Chong, C.K.: Rotational invariance in the three-dimensional lattice Boltzmann method is dependent on the choice of lattice. J. Comput. Phys. **230**(16), 6367–6378 (2011)